

Three-Dimensional Network Structure and Mechanical Properties of Al-Cu-Ni-Fe Cast Alloys with Gd Micro-addition



HUAWEI ZHANG, YUE LIU, and TONGXIANG FAN

High-temperature tensile testing and X-ray microscope (XRM) characterization were performed to assess the effects of the micro-addition of Gd and the three-dimensional (3-D) network structure on the improvement of Al-6Cu-3.5Ni-0.8Fe alloy under as-cast conditions. Gd addition contributed to the modification of the microstructure, where a new thermally stable micro-sized Al_3CuGd phase was formed, and the refinement occurred in Al_3CuNi and Al_9FeNi . The tensile test results revealed that the alloy modified with 0.4 pct Gd exhibited optimal properties at 623 K (350 °C), with an ultimate tensile strength, yield strength, and elongation of 74.1 MPa, 61.2 MPa, and 15.5 pct, respectively. Fractographic analysis after the tensile tests indicated that at ambient temperature, brittle cleavage-type fracture of the precipitates and ductile fracture of the matrix were dominant, whereas the transformation from mixed fracture to fully ductile trans-crystalline fracture was detected at elevated temperatures. According to the CT characterization, there was no significant difference in the curvature or interconnectivity of the 3-D network structure formed by the aluminides between before and after the tensile test at 623 K (350 °C). It is believed that the 3-D continuous network structure of aluminides, equipped with excellent heat resistance, plays a pivotal role in the high-temperature performance of the studied alloys. This work provides a new and promising idea for solving the current heat resistance problems of cast Al alloys.

<https://doi.org/10.1007/s11661-021-06254-0>

© The Minerals, Metals & Materials Society and ASM International 2021

I. INTRODUCTION

OWING to the pursuit of emission reduction and fuel utilization, light alloys, especially Al alloys, have gradually become mainstream.^[1–3] Because of their excellent properties, such as low density, high specific strength and stiffness, and good malleability, Al alloys are widely used in the automotive and aerospace industries, particularly in engine pistons.^[4–6] Unfortunately, above 473 K (200 °C), traditional enhancement phases, such as Al_2Cu and Mg_2Si , tend to coarsen and dissolve, which limits service at high temperatures.^[7,8] It is currently difficult to meet the high-temperature service demands of automobile engine pistons. Consequently,

there is an increasing need to develop new heat-resistant Al alloys.

It is widely recognized that alloying with various elements, such as Mg, Ni, Fe, and Mn, to form thermally stable intermetallic compounds is the most effective way to improve the elevated-temperature properties of Al alloys.^[9–18] Karnesky *et al.*^[19] reported that Al-0.08Sc and Al-0.06Sc-0.02Gd exhibited almost the same performance in terms of incubation time, peak hardness, and over-aging behavior. In addition, Zhang *et al.*^[20] found that a uniform and nanoscale Al_3CuGd phase formed in Al-Zn-MgZr alloys with Gd addition, which could pin dislocations and sub-grain boundaries to inhibit further recrystallization. Sui *et al.*^[21] reported that the addition of Gd to Al-12Si-4Cu-2Ni-0.8Mg alloys reduced the second dendrite arm spacing (SDAS), changed the morphology of the Ni-rich phases, and improved the mechanical properties at high temperatures. Therefore, Gd has the potential to replace expensive Sc to improve the high-temperature performance of Al alloys.

In fact, in addition to the types and sizes of intermetallics, their 3-D structures play a pivotal role in the high-temperature performance of Al alloys.^[22–30] Li *et al.*^[23] found that the consequent strip-like morphology was the most favorable morphology for

HUAWEI ZHANG and YUE LIU are with the State Key Laboratory of Metal Matrix Composites, Shanghai Jiao Tong University, 800 Dongchuan Road, Shanghai, 200240, P.R. China. TONGXIANG FAN is with the State Key Laboratory of Metal Matrix Composites, Shanghai Jiao Tong University and also with the State Key Laboratory for Metal Matrix Composites, School of Materials Science and Engineering, Shanghai Jiaotong University, Shanghai, 200240, P.R. China. Contact e-mail: txfan@sjtu.edu.cn

Manuscript submitted November 15, 2020; accepted March 17, 2021.

Article published online April 11, 2021

high-temperature strength enhancement, based on the examination of three Ni-containing phases. Asghar *et al.*^[24] reported that compared to an alloy without Ni addition, the modified AlSi₁₂Ni alloy showed ~ 50 pct higher strength at 573 K (300 °C) and ~ 30 pct longer thermal cycling life, owing to the hybrid three-dimensional (3-D) structures of aluminides and eutectic Si. In addition, Huang *et al.*^[31] observed 3-D hierarchical branched TiB_w and claw-like TiB_w structures in TiB_w/Ti₆Al₄V composites, which increased the maximum service temperature from 673 K to 873 K (400 °C to 600 °C). However, the mechanism through which the 3-D network structure strengthens the high-temperature strength of Al alloys has not yet reached a unified conclusion. Asghar *et al.*^[24,32] characterized the rigid multiphase network structure in AlSi₁₀Cu₅Ni₁ and AlSi₁₀Cu₅Ni₂ piston alloys by synchrotron tomography and concluded that the load transfer from the Al matrix to rigid phase was responsible for the high-temperature strength improvement. Yang *et al.*^[33] found that the TiC network constrained the α -Al matrix to form an overall deformation during a tensile test at high temperature, which was called the “constraint strengthening” mechanism. However, few studies have addressed the network structure strengthening mechanism by analyzing quantitative indices, such as the volume fraction of rigid phases, interconnectivity, contiguity, and morphology.

Thus, the objective of this study was to explore the relation between the 3-D network structure strengthening and high-temperature properties of Al alloys by analyzing the transformation of the network structure parameters (interconnectivity and curvatures) during a tensile test. The effect of Gd micro-addition on the microstructure and mechanical properties of Al-Cu-Ni-Fe cast alloys was also investigated systematically.

II. EXPERIMENTAL PROCESS

A. Alloy Processing

The main alloys studied in this work were Al-6Cu-3.5Ni-0.8Fe and modified alloys with Gd addition (0.1 to 0.4 wt pct), which were prepared by melting various master alloys along with pure Al, such as Al-50Cu, Al-10Ni, Al-10Fe, and Al-20Gd. All compositions are given as weight percentages in this report unless otherwise specified. Firstly, pure Al was melted in an electrical resistance furnace at 973 K (700 °C). Then, the master alloys mentioned above were added to the melt at 1023 K (750 °C), which had been preheated at 473 K (200 °C) for 2 hours. To ensure sufficient melting of the master alloys, the melt was stirred for 5 minutes and held at 993 K (720 °C) for 30 minutes. Refinement and degassing were conducted at 1013 K (740 °C). Finally, the melt was cooled to 973 K (700 °C) and poured into a metallic mold equipped with sprue. Table I presents the actual chemical compositions of the studied alloys, which were determined using inductively coupled plasma-atomic emission spectrometry.

B. Microstructure Characterization and Mechanical Testing

All of the metallographic specimens were cut from the same location as the as-cast ingots with different levels of Gd addition, approximately 10 mm above the bottom of the ingots. Then, grinding, polishing, and etching were performed according to standard specifications. The alloy samples for the metallographic investigations were ground using silicon carbide abrasive papers up to a grit number of 1500, polished using diamond grinding paste, and etched using Keller reagent (2.5 mL HNO₃, 1.5 mL HCl, 1 mL HF, and 95 mL distilled water) for 5 seconds. To explore the solidification process, differential scanning calorimetry (DSC, STA449-F3, NETZSCH, Germany) was performed at a heating rate of 10 K/min. X-ray diffraction (XRD, D8 DaVinci, Bruker, Germany) was performed to verify the phases in the as-cast alloys, and the results were analyzed using Jade software. During the test, Cu ($K\alpha$, $\lambda = 1.54056 \text{ \AA}$) was selected as the X-ray target with a 2θ range of 10 to 90 deg at a scan speed of 4 deg/min and scan step of 0.02 deg, and the voltage and current were configured as 40 kV and 15 mA, respectively. The microstructures of the studied alloys were examined under unetched conditions by scanning electron microscopy (SEM, VEGA3, TESCAN, Czech Republic) equipped with an energy dispersive spectrometer (EDS, AZtec MaxN-80, TESCAN, Czech Republic), and with a supply of 20.0 kV. In addition, an X-ray microscope (XRM, Xradia 520, Zeiss, Germany) was used to characterize the 3-D morphologies of the studied alloys in terms of the interconnectivity and curvatures, which were calculated using Avizo software. One thousand projections were obtained using an effective pixel size of $0.569 \mu\text{m}^2$ for 3-D reconstruction, whereas the source was equipped with a supply of 70.0 kV and power of 6 W.

In this study, dog-bone-shaped specimens were prepared according to the ISO 6892-1:2009 standard,^[34] which determined the specimen size to be $54.5 \times 15 \times 2$ mm. Tensile tests were performed at room temperature (298 K) using a Zwick/Roell Z100 testing machine, and at elevated temperatures (423, 473, 523, 573, and 623 K) using a Zwick/Roell Z050 testing machine with a deviation of ± 10 K and a constant speed of 0.5 mm/min. Before the high-temperature test, all the specimens were kept in the heating chamber of the Zwick/Roell Z050 testing machine for 30 minutes at the desired temperature. To ensure reliability, each test result given in this report is the average of the results for three tensile test specimens at the corresponding temperature.

III. RESULTS

A. Phase and Microstructural Analysis

Figure 1 shows the XRD patterns of the as-cast Al-6Cu-3.5Ni-0.8Fe alloys with and without 0.4 wt pct Gd addition. These results indicate that both of the alloys tested consist of α -Al, the T -Al₉FeNi phase, and three Ni-rich phases, specifically, the ϵ -Al₃Ni, γ -Al₇Cu₄Ni, and δ -Al₃CuNi phases. The typical phase

Table I. Chemical Composition of Cast Al-6Cu-3.5Ni-0.8Fe-xGd Alloys as Weight Percentages

Alloy	Cu	Ni	Fe	Mg	Mn	Gd	Al
#0	6.04	3.53	0.81	0.005	0.002	0.00	bal.
#1	6.10	3.61	0.79	0.003	0.001	0.08	bal.
#2	6.14	3.54	0.85	0.004	0.001	0.17	bal.
#3	6.02	3.59	0.84	0.003	0.001	0.26	bal.
#4	6.13	3.56	0.82	0.004	0.002	0.34	bal.

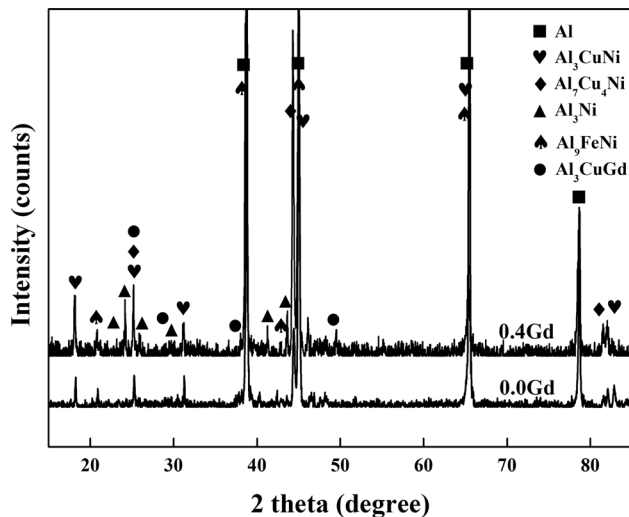


Fig. 1—XRD patterns of Al-6Cu-3.5Ni-0.8Fe alloys with and without 0.4 wt pct Gd addition.

composition has also been reported previously.^[17,25] Both Gumenuik^[35] and Raghavan^[36] stated that seven ternary compounds, $GdCu_{4.7-4.9}Al_{7.3-7.1}$ (τ_1), $GdCu_{7.8}Al_{3.2}$ (τ_2), $GdCu_{6.6}Al_{4.4}$ (τ_3), $Gd_2Cu_{9.4-6.7}Al_{7.6-10.3}$ (τ_4), $Gd_3Cu_{2.1}Al_{8.9}$ (τ_5), $GdCu_{0.9}Al_{2.1}$ (τ_6), and $GdCuAl$ (τ_7), were known in the Al-Cu-Gd system. In this study, the diffraction peak of Al_3CuGd was detected during the XRD test in the as-cast Al-6Cu-3.5Ni-0.8Fe alloys with 0.4 pct Gd addition, as also reported by Sui^[21] and Zhang.^[20] Because of the large homogeneity range revealed in Reference 35, Al_3CuGd can be considered a variant of $Gd_2Cu_{9.4-6.7}Al_{7.6-10.3}$ (τ_4). In addition, the diffraction peak of $\epsilon-Al_3Ni$ becomes more prominent after Gd addition, which can be interpreted as the substitution of Gd for Ni in $\delta-Al_3CuNi$ to form Al_3CuGd .

Figure 2 depicts the microstructures of the as-cast Al-6Cu-3.5Ni-0.8Fe alloys with different Gd contents. Table II gives the chemical compositions of the phases observed through EDS point analysis, along with the literature suggestions. From the SEM and EDS results, $\alpha-Al$ and five types of intermetallics were detected in the studied alloys. The $\epsilon-Al_3Ni$ phase (label 7) exhibits a gray flocculent-like morphology in Figures 2(d) through (f), and the $\gamma-Al_7Cu_4Ni$ phase (labels 2 and 8) exists in the form of a bright white lump type according to the SEM results. The $\delta-Al_3CuNi$ phase (labels 1 and 9) has a white skeleton-like morphology, in which the branches

become thinner and denser with the dissolution of Gd into them. Compared to the $\delta-Al_3CuNi$ phase labelled 9, the structure of the phase labelled 1 is significantly denser and more compact, being rich in 1.13 at. pct Gd. This phenomenon is consistent with the results reported by Sui.^[21] The gray plate-like intermetallic compound is T- Al_9FeNi (labels 4 and 5) on a large scale. Comparison of Figures 2(a) through (f) indicates that T- Al_9FeNi decomposes into smaller sizes and the edges become more rounded, marked by solid ellipses, with increasing Gd content. In other words, the Gd content plays a critical role in the morphologies of $\delta-Al_3CuNi$ and T- Al_9FeNi . More importantly, the Gd-rich phase (labels 3 and 6) with a bright white skeleton-like morphology appears along with the $\delta-Al_3CuNi$ phase, as marked by dotted ellipses in Figures 2(b) and (d).

Figure 3 shows the DSC curves of the as-cast Al-6Cu-3.5Ni-0.8Fe alloys with different Gd contents. Four main endothermic peaks in the studied alloys, marked as 1, 2, 3, and 4, respectively, can be recognized as follows^[37,38]: peak 1 is due to the formation of $\alpha-Al$, peak 2 may be attributed to the precipitation of the T- Al_9FeNi phase, peak 3 is considered to be the product of the $\delta-Al_3CuNi$ phase, and peak 4 is identified as the formation of the $\gamma-Al_7Cu_4Ni$ phase. In addition, the temperatures of peaks 2 and 3 decrease gradually with increasing Gd content, resulting in changes in the morphologies of $\delta-Al_3CuNi$ and T- Al_9FeNi , as shown in Figure 2. It is worth mentioning that there was no endothermic effect corresponding to the Al_3CuGd phase in the DSC results. This phenomenon was also reported by Sui.^[22] Considering that Ni was detected in the Gd-rich phase from the EDS results, it can be inferred that Al_3CuGd may be formed by replacing Ni with Gd in Al_3CuNi . In fact, the detailed precipitation of Al_3CuGd requires further exploration.

It is widely accepted that the high-temperature strength of an alloy is correlated with the thermal stability of the intermetallic phases. Both melting point and hardness can reflect the thermal stability of intermetallic phases. In view of the lack of the melting points, hardness is used in this work to further discuss the contribution of different intermetallic phases to the high-temperature performance of the studied alloys. Considering this fact, Table III lists the characteristics of the intermetallic phases detected in the studied alloys. According to the table, $\delta-Al_3CuNi$, T- Al_9FeNi , and $\gamma-Al_7Cu_4Ni$ always exhibit higher hardness at different temperatures. In addition, when the temperature rises to 623 K (350 °C), the hardness of $\gamma-Al_7Cu_4Ni$ drops sharply, whereas $\delta-Al_3CuNi$ and T- Al_9FeNi maintain their excellent hardness. Therefore, it can be inferred that, among all the intermetallic phases detected, $\delta-Al_3CuNi$ and T- Al_9FeNi contribute the most to the high-temperature strength of the studied alloys. On the other hand, Atwood *et al.*^[39] used in-house algorithms and codes to solve the problem of pore boundary segmentation, and successfully characterized both the pore size, interpore aperture size distributions and pore interconnectivity in bioactive glass foam tissue engineering scaffolds accurately. This work has provided great inspiration

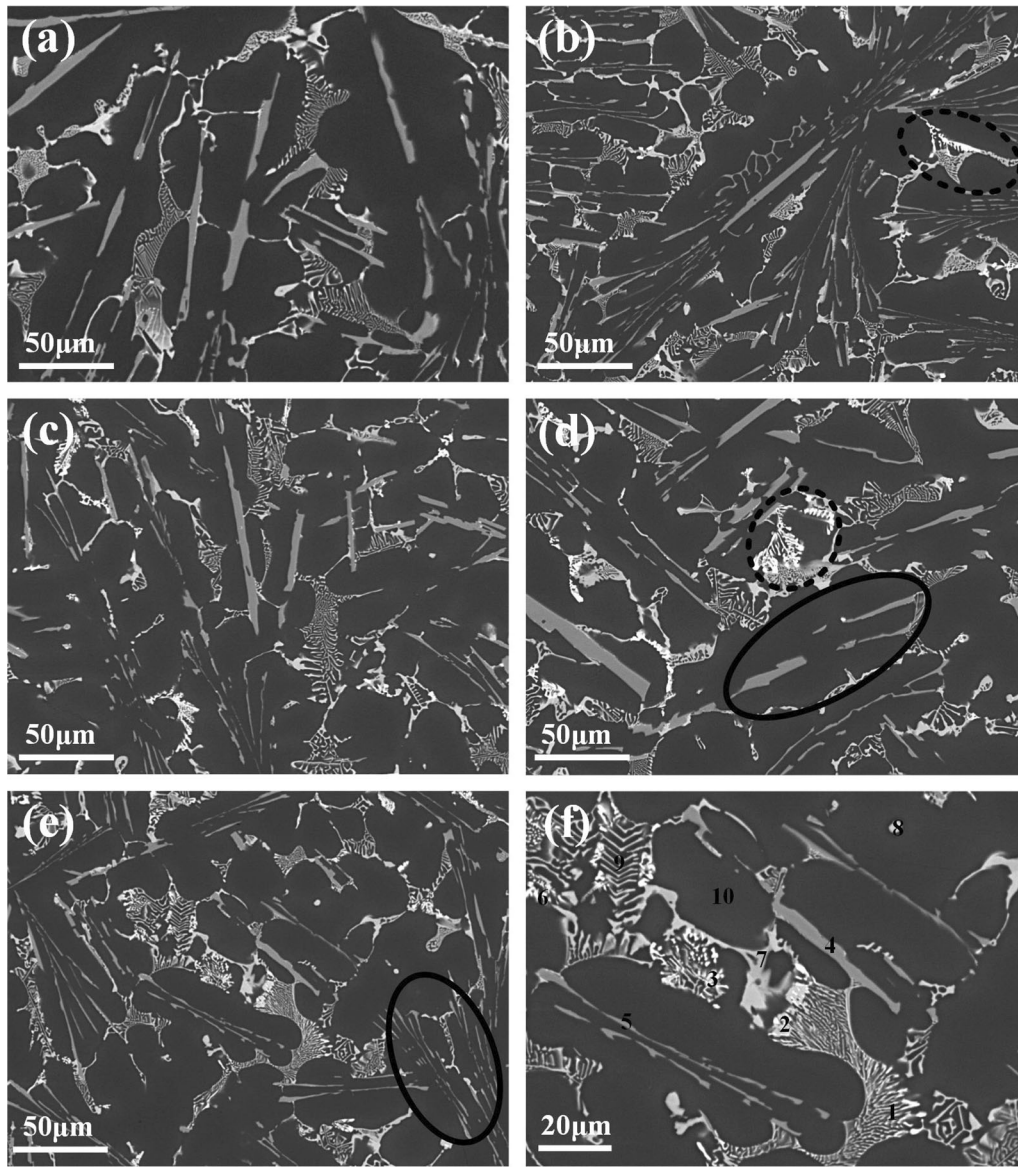


Fig. 2—Microstructures of Al-6Cu-3.5Ni-0.8Fe alloys with different levels of Gd addition: (a) 0 wt pct Gd, (b) 0.1 wt pct Gd, (c) 0.2 wt pct Gd, (d) 0.3 wt pct Gd, and (e) and (f) 0.4 wt pct Gd.

Table II. Chemical Compositions of Cast Al-6Cu-3.5Ni-0.8Fe-xGd Alloys

No.	Element Contents (At. Pct)					Phase
	Al	Cu	Ni	Fe	Gd	
1	65.25	18.30	15.32	0	1.13	Al ₃ CuNi
2	66.17	23.97	8.96	0	0.90	Al ₇ Cu ₄ Ni
3	76.70	18.22	1.75	0	3.32	Al ₃ CuGd
4	82.92	0.84	10.3	5.94	0	Al ₉ FeNi
5	88.88	1.24	6.73	3.15	0	Al ₉ FeNi
6	81.59	15.29	0.76	0	2.36	Al ₃ CuGd
7	72.47	0.57	26.96	0	0	Al ₃ Ni
8	69.99	25.33	4.44	0.24	0	Al ₇ Cu ₄ Ni
9	65.91	19.32	14.2	0.57	0	Al ₃ CuNi
10	98.86	1.02	0.12	0	0	Al-matrix

for our research. However, limited by the imaging principle of XRM and the closeness of the densities of intermetallic phases, it is currently not possible to effectively segment different intermetallic phases. We believe that it will be valuable and meaningful to characterize the volume fractions of different phases at room temperatures and high temperatures. For example, the relationship between the volume fraction and hardness of the intermetallic phases and their contribution to the alloy strength should be studied. In future work, we will try to effectively segment the intermetallic phases in the studied alloys and accurately calculate the volume fraction of each phase.

B. Mechanical Properties

The mechanical properties of as-cast alloys are determined by numerous factors, such as the elements added, casting technology, and solidification process.^[21,35] Figure 4 and Table IV present the ultimate tensile strength (UTS), yield strength (YS), and elongation (EL) of the studied alloys at different temperatures. As shown in Figure 4, the testing temperature in the range of 298 K to 623 K (25 °C to 350 °C) plays a decisive role in the strength and ductility. With increasing testing temperature, both the UTS and YS decrease monotonically, whereas the EL tends to increase linearly. The higher the temperature, the easier the dislocation movement owing to the domination of the thermally activated cross slip, which decreases the strength. Simultaneously, Al-matrix softening contributes to the increase in EL.^[40,41]

As shown in Figure 4(a), after modification by Gd addition, the UTS, YS, and EL all improve at 298 K (25 °C). The best tensile results occur with 0.4 pct Gd addition, with which the UTS, YS, and EL increase by 35.3 MPa, 31.6 MPa, and 1.2 pct, respectively. Further, the effect of Gd addition on the mechanical properties of

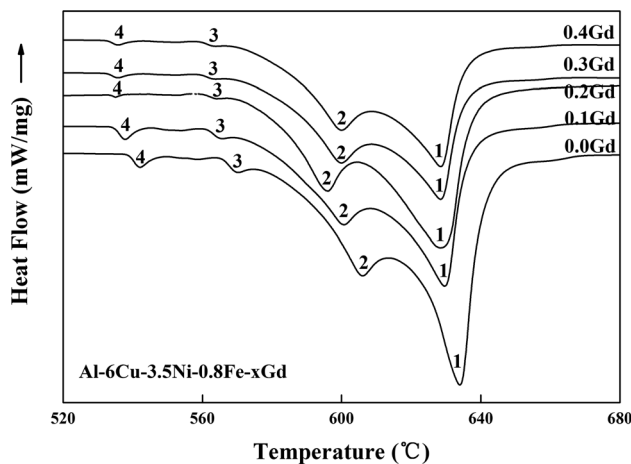


Fig. 3—DSC curves of Al-6Cu-3.5Ni-0.8Fe alloys with different Gd contents.

the studied alloys at 423 K (150 °C) agrees with that at room temperature. According to Figure 4(b), the UTS, YS, and EL are enhanced by ~ 12.9, ~ 16.7, and ~ 25 pct, respectively, in the alloy modified with 0.4 pct Gd compared with the untreated alloy at 423 K (150 °C). However, at testing temperatures between 423 K and 573 K (150 °C and 300 °C), the effects of Gd addition on the strength and ductility are less obvious than those in Figures 4(c) and (d). There is no distinct difference between the tensile results of the studied alloys with and without Gd addition at 473 K (200 °C) or 523 K (250 °C). As shown in Figure 4(e), when the Gd content increases from 0 to 0.4 wt pct, the UTS and YS increase by ~ 4.4 and ~ 6.2 pct at 573 K (300 °C), respectively. In addition, the UTS and YS are improved by ~ 10.0 and ~ 13.5 pct, respectively, in the alloy modified with 0.4 wt pct Gd compared with the base alloy at 623 K (350 °C). These changes are both greater than the results obtained at 573 K (300 °C). It can be concluded that Gd addition very positively affects the strength of the studied alloy at low temperatures (298 K to 423 K (25 °C to 150 °C)) and high temperatures (above 623 K (350 °C)), whereas the strengthening effect at medium temperatures (473 K to 573 K (200 °C to 300 °C)) is less obvious.

C. Fractography

To investigate further the failure mechanisms of the studied alloys at different temperatures, the fracture surfaces of each tested specimen were characterized by SEM. Figures 5 and 6 depict the fractography results of the specimens after tensile testing at 298 K (25 °C) and 623 K (350 °C), respectively. It is widely recognized that voids that form between the intermetallics and matrix due to the critical stress or debonding play a decisive role in the fracture process. Casting defects, especially internal pores, dry oxide, and shrinkage, are also susceptible to crack nucleation.^[3,14]

After tensile testing at ambient temperature (298 K (25 °C)), the fracture surfaces of all specimens exhibit intergranular features along with some large flat areas, especially cleavage-type fractures in the plate-type intermetallics. Figure 5(d) shows distinct river patterns, which are indicated by dotted rectangles. It is obvious that the black cleavage plane (marked by dotted

Table III. Characteristics of the Intermetallic Phases in Cast Al-6Cu-3.5Ni-0.8Fe-xGd Alloys^[22]

Phase	Crystal Structure	Symbol	Density (g cm ⁻³)	Hardness (GPa)		
				25 °C	200 °C	350 °C
Al	Cubic	α	2.70	1.45 ± 0.17	0.68 ± 0.10	0.143 ± 0.005
Al ₂ Cu	Tetragonal	θ	4.34	5.77 ± 0.91	5.33 ± 0.20	2.48 ± 0.32
Al ₃ CuNi	Hexagonal	δ	4.76	10.45 ± 0.76	9.48 ± 0.55	6.46 ± 0.69
Al ₇ Cu ₄ Ni	Trigonal	γ	5.48	9.25 ± 0.75	8.22 ± 0.73	4.86 ± 1.20
Al ₃ Ni	Orthorhombic	ϵ	3.95	5.95 ± 0.75	—	3.54 ± 0.69
Al ₉ FeNi	Monoclinic	T	3.4	7.71 ± 0.58	6.96 ± 0.31	5.83 ± 0.31
Al ₃ CuGd	Hexagonal	—	4.95	—	—	—

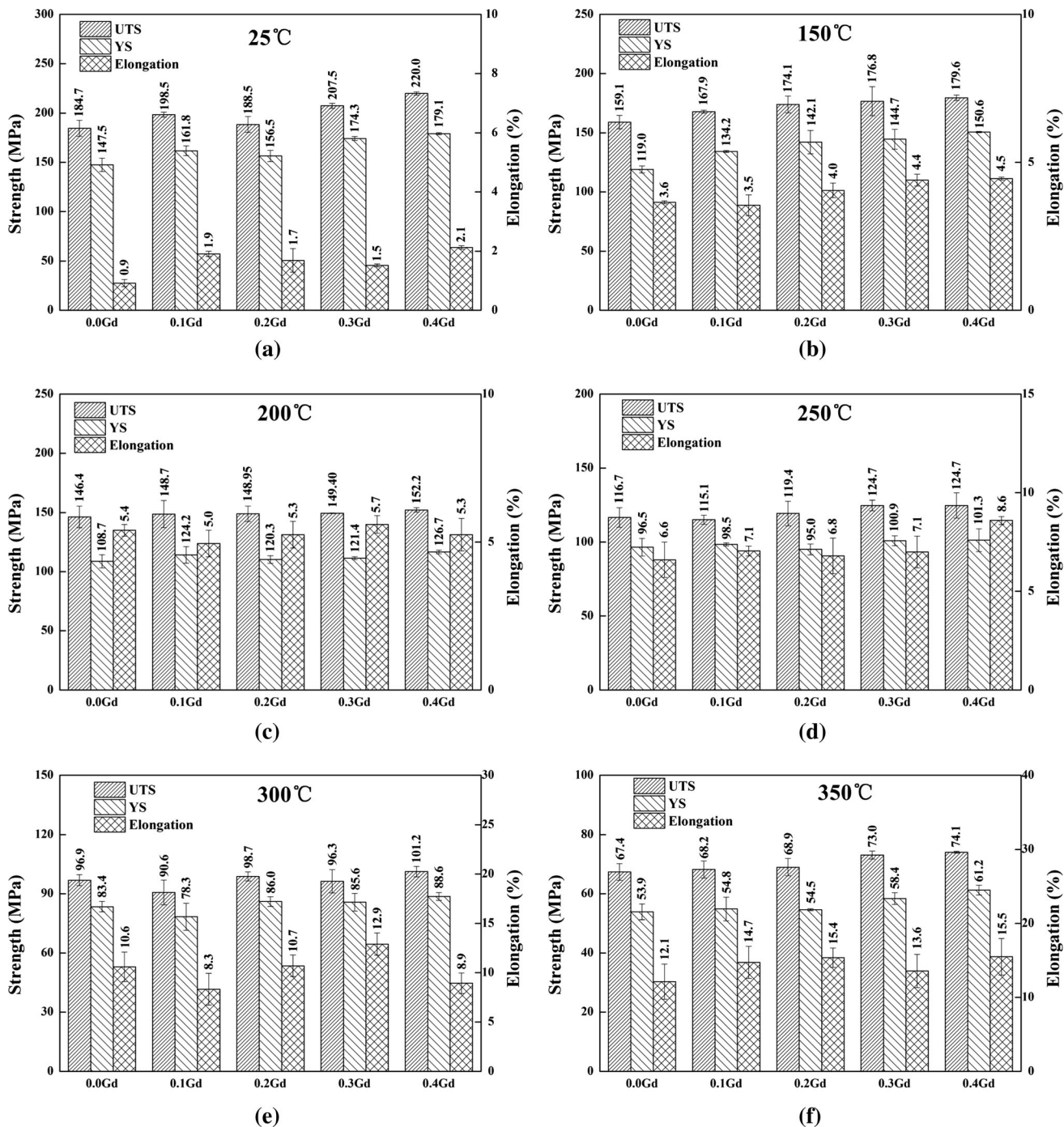


Fig. 4—Tensile properties of Al-6Cu-3.5Ni-0.8Fe alloys with and without Gd addition at different temperatures: (a) 298 K (25 °C), (b) 423 K (150 °C), (c) 473 K (200 °C), (d) 523 K (250 °C), (e) 573 K (300 °C), and (f) 623 K (350 °C).

arrows) gradually becomes smaller and exhibits a more scattered distribution with increasing Gd addition. Figure 5(f) shows the EDS results of the cleavage plane labeled with a star in Figure 5(c). It can be determined that the black cleavage plane is mostly formed from Fe-rich phases, especially the T-Al₉FeNi phase. In addition, many secondary cracks (indicated by solid arrows) appear on the cleavage plane owing to the stress concentration. This morphology suggests that there is an intensive interaction between the

plastic flow or slip bands and the Fe-rich phases, especially at the grain boundaries, which leads to the initiation of intergranular cracking. It is worth noting that the gray cleavage planes (labeled by solid rectangles) appear after the Gd content exceeds 0.2 wt pct, which has a high probability of being a Gd-rich phase according to the SEM microstructure in Figure 2. A similar fracture phenomenon was also reported previously^[20,21] for an alloy modified with the addition of Gd and Fe during tensile loading.

Table IV. Tensile Properties of Al-6Cu-3.5Ni-0.8Fe Alloys With and Without Gd Addition at Different Temperatures

Temperature	Property	Gd Addition (Wt Pct)				
		0.0	0.1	0.2	0.3	0.4
298 K (25 °C)	UTS (MPa)	184.7	198.5	188.5	207.5	220.0
	YS (MPa)	147.5	161.8	156.5	174.3	179.1
	EL (pct)	0.9	1.9	1.7	1.5	2.1
423 K (150 °C)	UTS (MPa)	159.1	167.9	174.1	176.8	179.6
	YS (MPa)	119.0	134.2	142.1	144.7	150.6
	EL (pct)	3.6	3.5	4.0	4.4	4.5
473 K (200 °C)	UTS (MPa)	146.4	148.7	148.9	149.4	152.2
	YS (MPa)	108.7	124.2	120.3	121.4	126.7
	EL (pct)	5.4	5.0	5.3	5.7	5.3
523 K (250 °C)	UTS (MPa)	116.7	115.1	119.4	124.7	124.7
	YS (MPa)	96.5	98.5	95.0	100.9	101.3
	EL (pct)	6.6	7.1	6.8	7.1	8.6
573 K (300 °C)	UTS (MPa)	96.9	90.6	98.7	96.3	101.2
	YS (MPa)	83.4	78.3	86.0	85.6	88.6
	EL (pct)	10.6	8.3	10.7	12.9	8.9
623 K (350 °C)	UTS (MPa)	67.4	68.2	68.9	73.0	74.1
	YS (MPa)	53.9	54.8	54.5	58.4	61.2
	EL (pct)	12.1	14.7	15.4	13.6	15.5

In Figure 6(a), the test specimen without Gd addition exhibits the coexistence of brittle fracture and ductile fracture at 623 K (350 °C), with cleavage planes and tear ridges (labeled by arrows). However, fully ductile trans-crystalline fracture is observed in the other specimens modified by Gd addition at the same temperature, which is distinguished by numerous tear ridges and dimples. The most important effect of high temperature is that the interfacial bonding between the matrix and intermetallics becomes weaker. When the temperature rises, owing to the large difference in thermal expansion, a stress gradient forms, leading to the pull-out of the intermetallics. In Figure 6(e), the pull-out of the T-Al₉FeNi phase is indicated by dotted rectangles, which still exhibit few secondary cracks. The numerous micro-voids distributed on the fracture surface in Figure 6 also confirm the theory mentioned above. It is worth noting that there are extensive fragments in the dimples in Figure 6(f), which were identified as Gd-rich phases through EDS analysis.

Figures 7 and 8 present SEM micrographs of the polished cross-sections of the studied alloys after the tensile tests at 298 K (25 °C) and 623 K (350 °C), respectively. As seen in Figure 7, a large amount of the T-Al₉FeNi phase is fractured near the fracture surface tested at room temperature. Because of the strong interface bonding between the high-aspect-ratio T-Al₉FeNi phase and α -Al matrix, many secondary cracks are observed in the T-Al₉FeNi phase, as indicated by the dotted arrows. In addition, the strong effect of the stress concentration contributes to the complete fragmentation of the T-Al₉FeNi phase, as indicated by the solid arrows in Figure 7. It can be determined that cracks nucleated and grew from the T-Al₉FeNi phase, leading to the overall fracture of the studied alloys during tensile testing at room temperature. At a testing

temperature of 623 K (350 °C), there are few secondary cracks, and the shatter of the T-Al₉FeNi phase cannot be observed in Figure 8. In contrast, de-cohesion and pull-out of the T-Al₉FeNi phase are evident (marked by solid arrows) because of the weak interface with the α -Al matrix. In addition, the intermetallics are displaced from their original positions and aligned with the tensile load direction, as can be clearly seen in Figure 8(e). In other words, the studied alloys can maintain cooperative deformation between the intermetallics and α -Al matrix during tensile testing at elevated temperatures.

D. 3-D Morphology

In this work, an X-ray microscope (XRM) was used to restructure the 3-D morphologies of the intermetallics using Avizo software. To reveal the effects of the network structure on the high-temperature strengths of the studied alloys, we also characterized Al-6Cu-3.5Ni alloy as a contract, which has not previously been reported to have an obvious 3-D network structure. In addition, the tested specimen of Al-6Cu-3.5Ni-0.8Fe-0.4Gd at 623 K (350 °C) was examined to explore the thermal stability of the network structure.

Figure 9 shows original cropped 100 μm \times 100 μm slices of Al-6Cu-3.5Ni and Al-6Cu-3.5Ni-0.8Fe-0.4Gd obtained by CT. It can be observed that the intermetallics in Al-6Cu-3.5Ni are of an intermittent lump type, which was identified as ϵ -Al₃Ni with a small amount of γ -Al₇Cu₄Ni and δ -Al₃CuNi in our previous study. The microstructure in Figure 9(b) is basically the same as that in Figure 2(e). In Figure 9(c), there is slight fracturing and stretching of the intermetallic dendrites in Al-6Cu-3.5Ni-0.8Fe-0.4Gd. However, the intermetallic network structure remains after tensile testing at 623 K (350 °C).

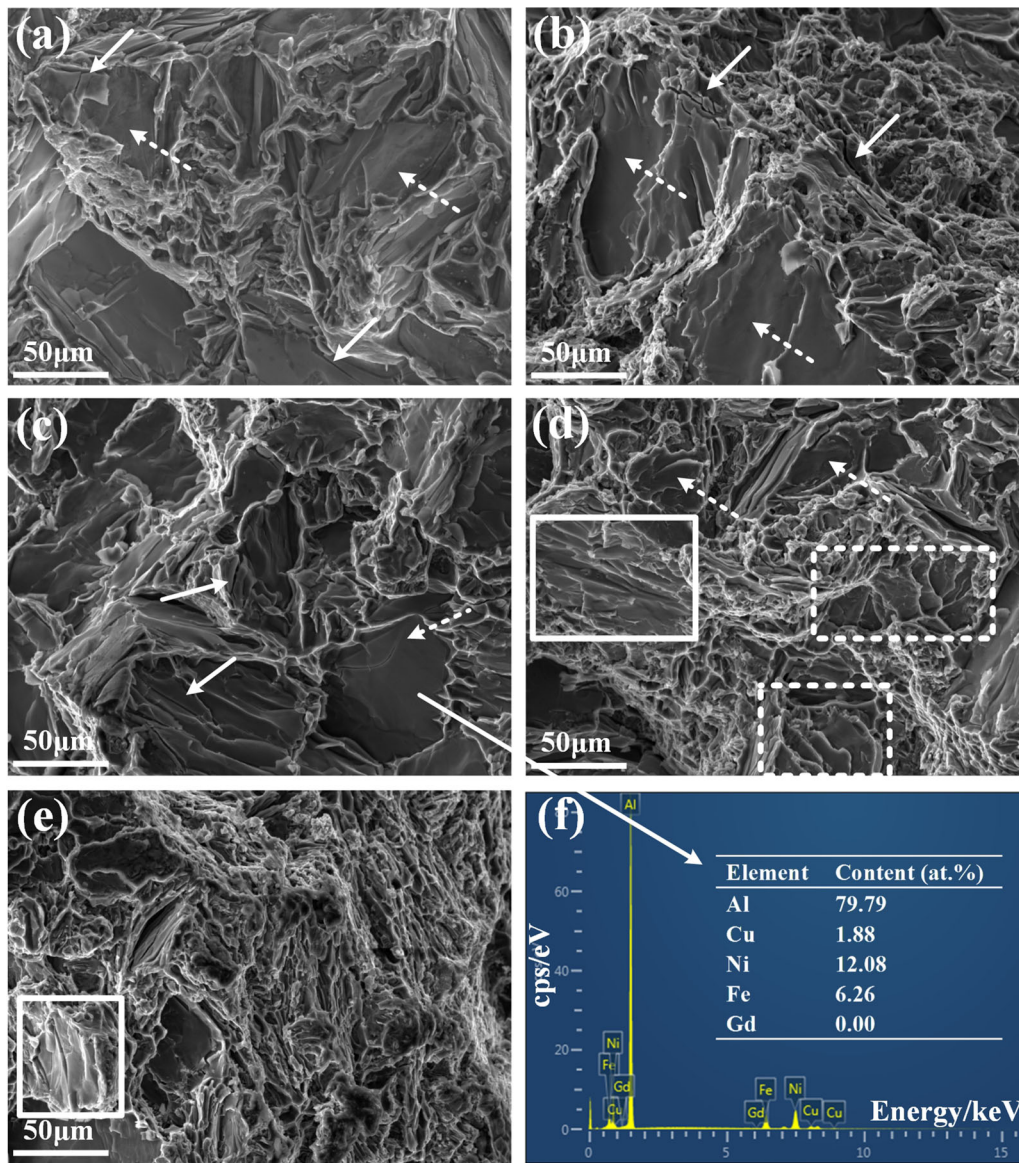


Fig. 5—SEM micrographs of fractured surfaces on the tensile specimens with different levels of Gd addition at 298 K (25 °C): (a) 0 wt pct Gd, (b) 0.1 wt pct Gd, (c) 0.2 wt pct Gd, (d) 0.3 wt pct Gd, (e) 0.4 wt pct Gd, and (f) EDS results of the marked point in (c).

Figure 10 shows the 3-D rendered volumes of the largest aluminide particles in Al-6Cu-3.5Ni and Al-6Cu-3.5Ni-0.8Fe-0.4Gd under different conditions. Table V lists the quantitative indicators, such as the volume fraction of all aluminides, interconnectivity, and contiguity obtained by Avizo software. According to References 24 and 32, interconnectivity is defined as the relative volume fraction of the largest particle of one intermetallic with respect to the total volume fraction of that phase in the analyzed range. Such a particle is recognized as an individual continuous 3-D region of a certain phase. Therefore, the largest particle of the analyzed phase was identified as the region with the largest volume fraction in the entire reconstructed region. This special formula can be expressed as follows:

$$\text{Interconnectivity} = \frac{\text{Volume of the largest particle of the phase}}{\text{Total volume of the phase}} \times 100 \text{ Pct.} \quad [1]$$

In this study, image grayscale was adopted as the discrimination criterion for various second phases. The specific algorithms and procedures were implemented by internal scheduling in Avizo. Further, the interconnectivity calculation was performed automatically using Avizo. To ensure reliability, each test result given in this report was obtained by averaging over more than 10 different fields.

With supernumerary addition of 0.8 wt pct Fe and 0.4 wt pct Gd, the volume fraction of aluminides in Al-6Cu-3.5Ni-0.8Fe-0.4Gd is ~ 4.3 pct higher than that

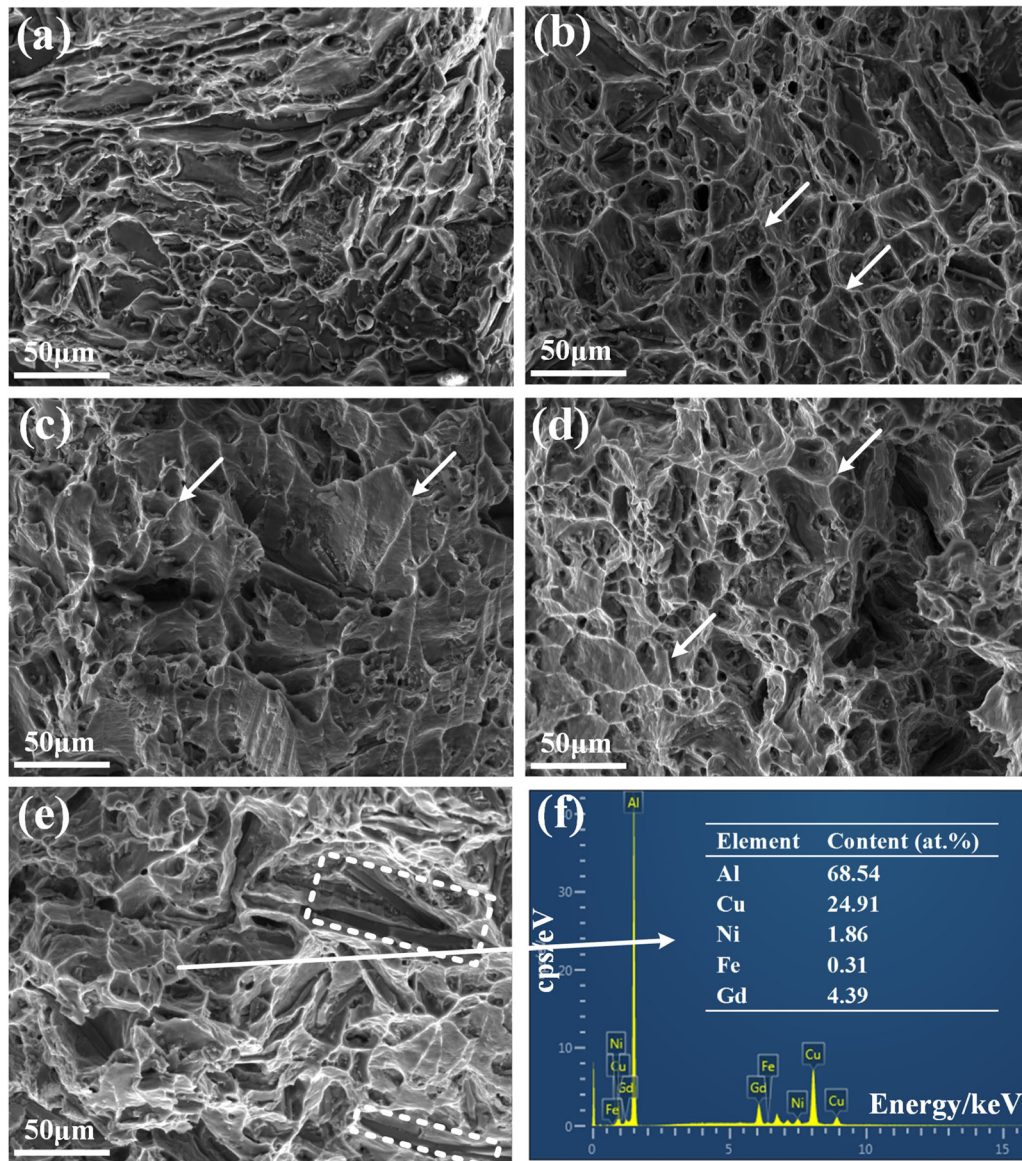


Fig. 6—SEM micrographs of fractured surfaces on the tensile specimens with different levels of Gd addition at 623 K (350 °C): (a) 0 wt pct Gd, (b) 0.1 wt pct Gd, (c) 0.2 wt pct Gd, (d) 0.3 wt pct Gd, (e) 0.4 wt pct Gd, and (f) EDS results of the marked point in (e).

in Al-6Cu-3.5Ni, which may contribute to the form of the network structure. There is no significant difference between the aluminide volume fractions before and after the tensile test in Al-6Cu-3.5Ni-0.8Fe-0.4Gd. However, after the tensile test at 623 K (350 °C), the interconnectivity decreases to ~ 96 pct from its previous value of ~ 98 pct. In other words, external stress negatively affects the completeness of the aluminide network structure during high-temperature tensile testing.

Surface curvature is a pivotal factor in morphology transformation because it indicates local variations in the surface energy. In fact, a 3-D surface can be described by two principal curvatures.^[42] They are defined as the minimum and maximum curvatures, which are called k_1 and k_2 , respectively, of the intersection between a plane containing the normal and surface. Combined with k_1 and k_2 , the Gaussian curvature K and

mean curvature H appear as follows and are widely used to characterize the shapes of rigid phases.

The Gaussian curvature is the product of the two principal curvatures:

$$K = k_1 \times k_2, \quad [2]$$

whereas the mean curvature is the mean value of the two principal curvatures:

$$H = \frac{1}{2} \times (k_1 + k_2). \quad [3]$$

Figure 11 presents the distributions of the Gaussian and mean curvatures of the aluminides analyzed using Avizo. In Figure 11(a), there is an ellipse-like distribution tendency around the point (0.1, 0) of curvatures in Al-6Cu-3.5Ni. Therefore, it can be inferred that the

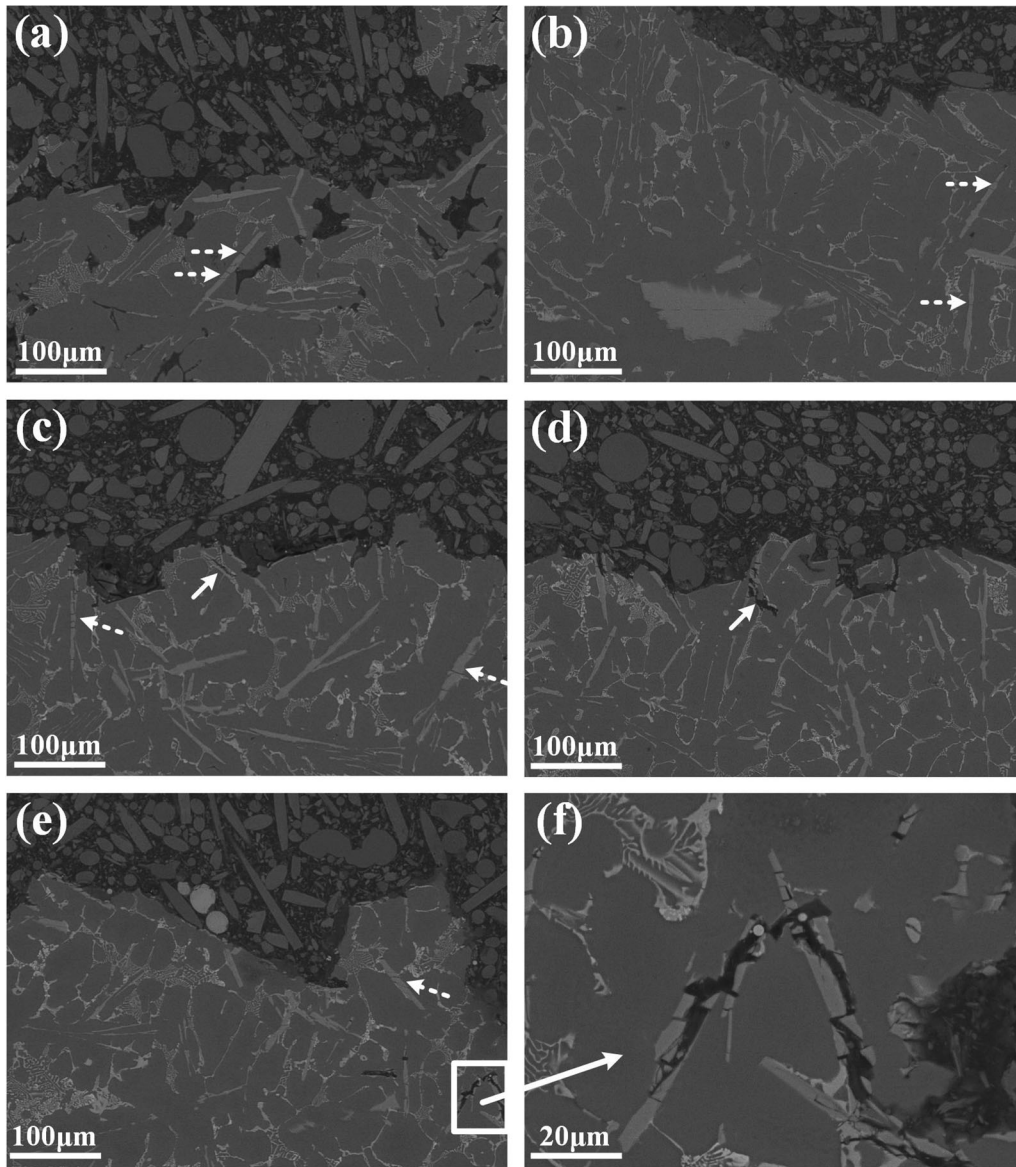


Fig. 7—SEM micrographs of polished cross-sections of the tensile fractured specimens with different levels of Gd addition at 298 K (25 °C): (a) 0 wt pct Gd, (b) 0.1 wt pct Gd, (c) 0.2 wt pct Gd, (d) 0.3 wt pct Gd, and (e) and (f) 0.4 wt pct Gd.

surfaces of the aluminides in Al-6Cu-3.5Ni mostly exhibit convex cylindrical, convex saddle, and spheroid types. All of the surfaces of the aluminides mentioned above interact with the matrix accompanied by large ups and downs, which harms the high-temperature strength of the alloy, as listed in Table V. There was no significant difference in the curvatures of the aluminides before and after the tensile test in Al-6Cu-3.5Ni-0.8Fe-0.4Gd. In other words, the continuous network structure formed by the aluminides has excellent heat resistance and rigidity, which can remain almost the same during tensile testing at elevated temperatures. In Figures 11(b) and (c), a maximum can be observed close to (0, 0) but the Gaussian curvature remains slightly negative. It can be determined that the surface features of the aluminides in Al-6Cu-3.5Ni-0.8Fe-0.4Gd may be flat-like, sometimes with rather flat symmetric

saddle-like features, leading to a simple and stable interaction with the matrix.

IV. DISCUSSION

A. Effects of Gd Addition on Mechanical Properties

Based on the analysis in Section III-B, it was inferred that Gd addition very positively affects the strength of the studied alloy at low temperatures (298 K to 423 K (25 °C to 150 °C)) but that this effect is less obvious at high temperatures (over 423 K (150 °C)). In fact, Gd affects the mechanical properties of the studied alloy by modifying its microstructure and forming a Gd-rich phase.

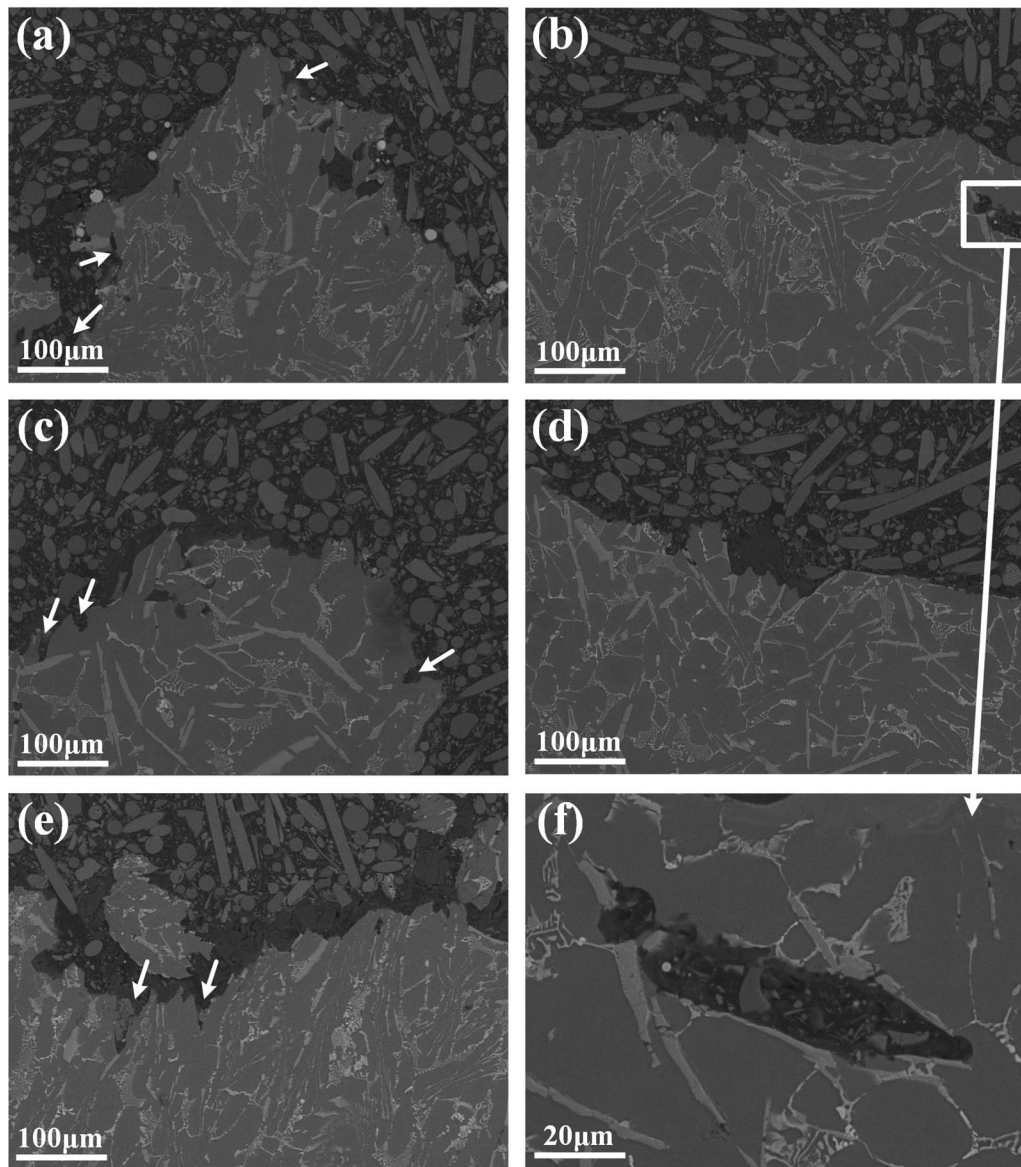


Fig. 8—SEM micrographs of polished cross-sections of the tensile fractured specimens with different levels of Gd addition at 623 K (350 °C): (a) 0 wt pct Gd, (b) and (f) 0.1 wt pct Gd, (c) 0.2 wt pct Gd, (d) 0.3 wt pct Gd, and (e) 0.4 wt pct Gd.

The most important factor affecting room-temperature strength is microstructure modification by Gd. As mentioned before, the decomposition and passivation of the T-Al₉FeNi phase relieve the stress concentration tendency, which may be the reason for the improvement of the mechanical properties at ambient temperature. On the other hand, it is widely accepted that the high-temperature strength is mainly determined by the intermetallic properties, such as size, distribution, morphology, and thermal stability. After modification by Gd, the T-Al₉FeNi phase in the microstructure develops into a small strip type from a large plate type and exhibits edge passivation, which can relieve stress concentration and reduce crack initiation. In addition, the branches of the δ -Al₃CuNi phase became smaller and denser as the Gd content increased, whereas the structural interconnectivity of the phases increased

correspondingly. Interconnectivity is a critical parameter affecting the strengthening of thermally stable phases.^[25] Sui^[43] and Zhang^[20] reported that Al₃CuGd was formed at the grain boundary in Al-Si-Cu-Ni-Mg-Gd and Al-Zn-Mg-Cu-Zr-0.1Gd. Further, it was confirmed that the Al₃CuGd phase can remain without coarsening and dissolving at 573 K to 673 K (300 °C to 400 °C).^[21] Both of these phenomena indicate that Al₃CuGd has excellent thermal stability and can impede the sliding of grain boundaries and hinder the deformation of the α -Al matrix. However, in this work, we attributed the improvement of the high-temperature mechanical properties at 623 K (350 °C) to the continuous 3-D network structure of the intermetallics, instead of the form of the Al₃CuGd phase. There is no distinct difference between the tensile

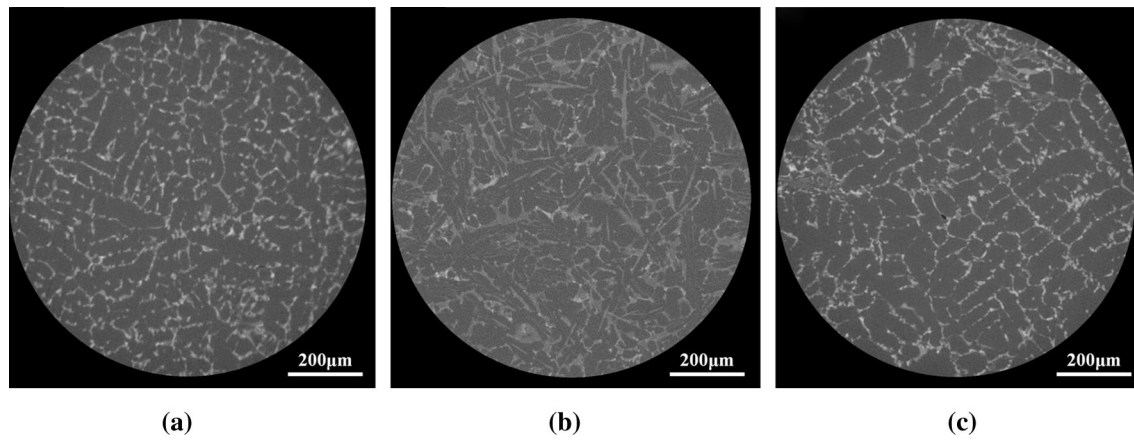


Fig. 9—CT slices of (a) Al-6Cu-3.5Ni alloy, (b) Al-6Cu-3.5Ni-0.8Fe-0.4Gd alloy, and (c) Al-6Cu-3.5Ni-0.8Fe-0.4Gd alloy after tensile testing at 623 K (350 °C).

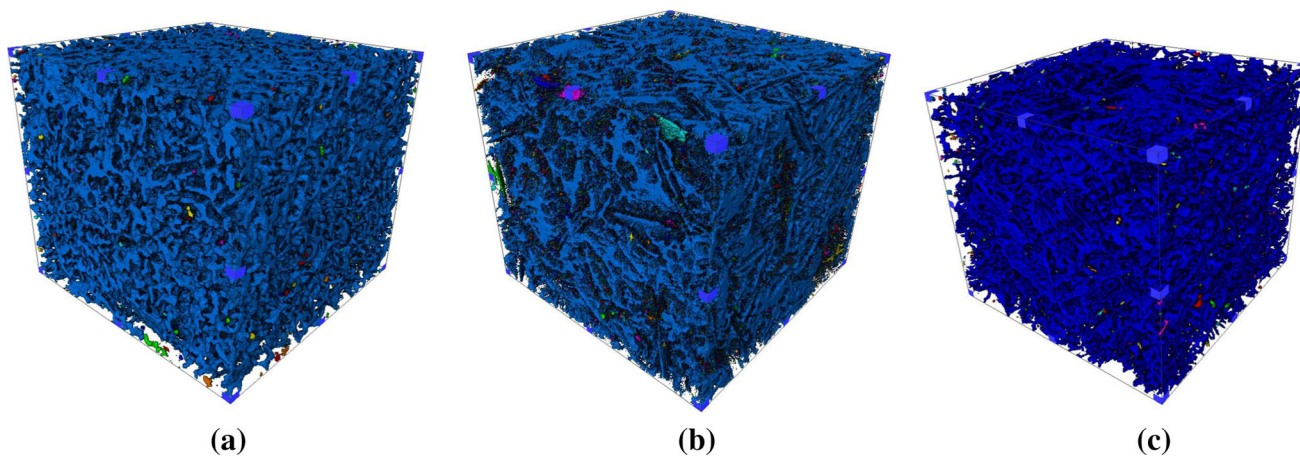


Fig. 10—Rendered structures of aluminides in (a) Al-6Cu-3.5Ni, (b) Al-6Cu-3.5Ni-0.8Fe-0.4Gd, and (c) Al-6Cu-3.5Ni-0.8Fe-0.4Gd after tensile testing at 623 K (350 °C).

Table V. Relative Quantitative Indicators of All Aluminides in Al-6Cu-3.5Ni-0.8Fe-0.4Gd and Al-6Cu-3.5Ni-0.8Fe-0.4Gd Under Different Conditions

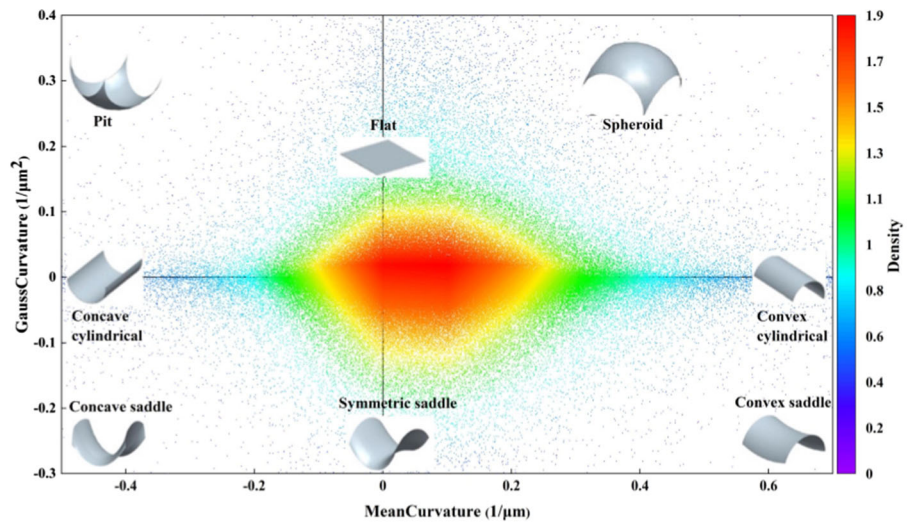
Alloy	Volume Fraction (Pct)	Interconnectivity (Pct)	UTS at 623 K (MPa)	YS at 623 K (MPa)
Al-6Cu-3.5Ni	17.8 ± 1.2	94 ± 1	62.6 ± 3.3	48.7 ± 2.4
Al-6Cu-3.5Ni-0.8Fe-0.4Gd	22.1 ± 1.1	98 ± 1	74.1 ± 1.2	61.2 ± 2.1
Al-6Cu-3.5Ni-0.8Fe-0.4Gd-fractured	22.0 ± 1.5	96 ± 2	74.1 ± 1.2	61.2 ± 2.1

results of the studied alloys with and without the Al_3CuGd phase at 473 K (200 °C) or 523 K (250 °C).

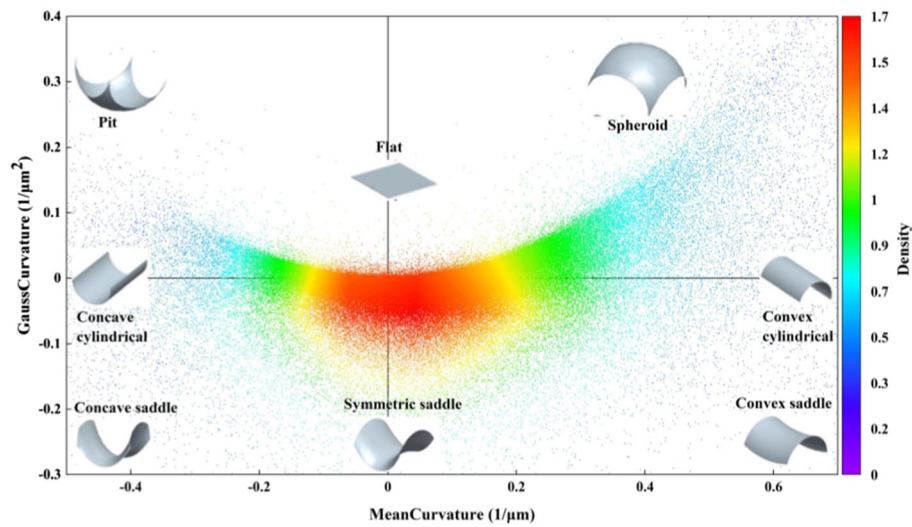
B. Effect of 3-D Continuous Network Structure on High-Temperature Strength

Based on the expression in Section III-B, the results confirm that the 3-D continuous network structure of aluminides plays a pivotal role in the high-temperature performance of alloys, which is determined by the volume fraction, interconnectivity, and curvatures.

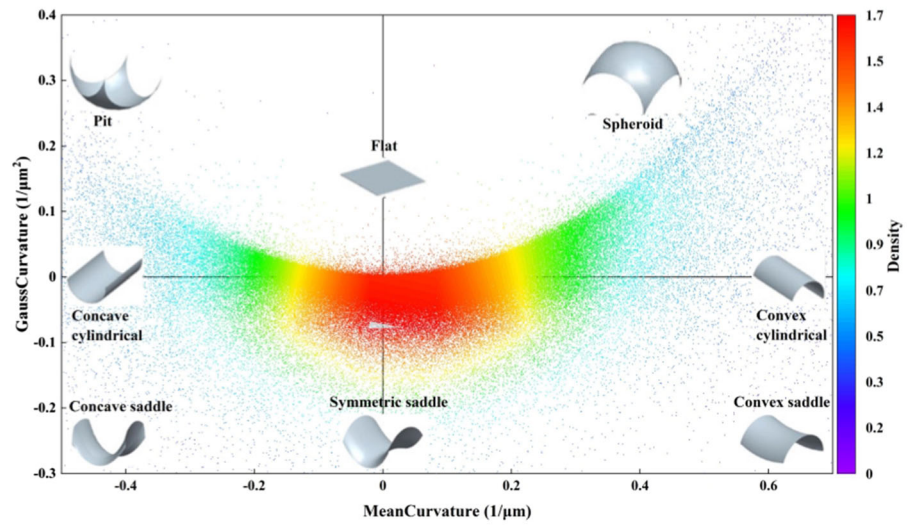
According to the Hashin and Shtrikman (H-S) theorem, the higher the volume fraction of the reinforcement, the greater the elastic modulus of the material. In many previous studies, various alloys and composites were designed based on the rigorous correspondence of the upper bound of the H-S theorem to composites containing the “soft” inclusion matrix phase encapsulated by a “stiffer” reinforcement phase. For the studied alloys in this work, intermetallics act as the stiffer reinforcement, and $\alpha\text{-Al}$ plays the part of the soft inclusion matrix. In addition, the interconnectivity plays



(a)



(b)



(c)

Fig. 11—Mean and Gaussian curvatures of aluminides in (a) Al-6Cu-3.5Ni, (b) Al-6Cu-3.5Ni-0.8Fe-0.4Gd, and (c) Al-6Cu-3.5Ni-0.8Fe-0.4Gd after tensile testing at 623 K (350 °C).

a virtual role in the stability of the 3-D continuous network structure of intermetallics, especially at high temperatures. As reported in Reference 32, high interconnectivity can result in an additional increase in load transfer from the matrix to the reinforcement, which is more important at high temperatures at which the matrix becomes softer. Finally, the curvature of the intermetallics can reflect their aspect ratio, which determines the effects of the load transfer from the Al matrix to the rigid phases. Owing to the large volume fraction, high interconnectivity, and flat surface of the 3-D network structure of aluminides, Al-6Cu-3.5Ni-0.8Fe-0.4Gd has an ~ 18.4 pct higher elevated-temperature strength than Al-6Cu-3.5Ni.

C. Strengthening Mechanism of the Studied Alloys

In fact, various factors, such as the type of elements added, intermetallic properties, and 3-D network structure, contribute successfully to the enhancement of the high-temperature strength of the studied alloys. The strengthening mechanisms responsible for the high-temperature strength of the studied alloys are as follows:

(a) Strain-hardened regions appear in the α -Al matrix along with the interface with intermetallics, such as Fe- and Ni-rich phases. This characteristic can be identified by the huge differences in the coefficients of thermal expansion (CTEs) and elastic moduli (EMs) of the α -Al matrix and intermetallics.^[44] Consequently, the production and proliferation of geometrically necessary dislocations (GNDs) occur gradually at the interface between the α -Al matrix and intermetallics during processing and testing.

The enhancement in the yield strength of the studied alloys $\Delta\sigma_{CTE}$, due to the CTE mismatch, is given by the following equation^[44-47]:

$$\Delta\sigma_{CTE} = 2 \times A \times M \times G \times b_m \times \left[\frac{3\sqrt{2} \times \Delta\alpha_C \times \Delta T \times V_i}{b_m \times d_i \times (1 - V_i)} \right]^{1/2}, \quad [4]$$

where A is a constant related to the transparency of the dislocation forest for basal-basal dislocation interactions in the α -Al matrix and M is the Taylor factor. According to Reference 47, the product of A and M can be treated as 1.25. G and b_m are the shear modulus (25.4 GPa at 298 K and 20.9 GPa at 623 K) and burgers vector (0.286 nm) of the α -Al matrix, respectively. V_i and d_i are the volume fractions (~ 22 pct) and diameters (~ 10 μ m) of the intermetallics acting as reinforcement. ΔT is the difference between the processing and test temperatures. $\Delta\alpha_C$ is the difference in CTE between the α -Al matrix and intermetallics. According to the results calculated using JMatPro, the CTEs of α -Al, T-Al₃FeNi, and δ -Al₃CuNi at 623 K (350 °C) are 0.0000258 °C⁻¹, 0.0000245 °C⁻¹, and 0.0000219 °C⁻¹, respectively.

The improvement in yield strength of the studied alloys $\Delta\sigma_{EM}$, owing to the EM mismatch, is given by the following equation^[44,48]:

$$\Delta\sigma_{EM} = A \times M \times G \times b_m \times \left[\frac{6 \times \varepsilon \times V_i}{b_m \times d_i} \right]^{1/2}, \quad [5]$$

where ε is the elastic strain at yield, which is treated as 0.002.

Considering that the recrystallization temperature of Al alloy is 623 K to 673 K (350 °C to 400 °C), Eqs. [4] and [5] cannot be used to calculate the strengthening effect of GNDs at 623 K (350 °C).

(b) The movement of dislocations was hindered by the rigid intermetallics, and a dislocation loop occurred, leading to the difficulty of deformation up to a large strain. The strengthening mechanism mentioned above is called the Orowan mechanism, which can be explained by the following equation^[44,45,49]:

$$\Delta\sigma_{OL} = \frac{0.4 \times M \times G \times b_m \times \ln(d_i/b_m)}{\pi \times d_i \times \left[2 \times (1/(\pi \times V_i))^{1/2} - 1 \right] \times (1 - \nu_m)^{1/2}}, \quad [6]$$

where ν_m is the Poisson's ratio of the α -Al matrix, which is treated as 0.345. Because of the large value of d_i , $\Delta\sigma_{OL}$ was calculated to be only 1.3 KPa at 623 K (350 °C).

(c) The load is transferred from the soft α -Al matrix to the rigid intermetallics through interface shear stress, which is usually called the load-bearing effect.^[50] The core of the mechanism is the load-carrying capacity of the intermetallics, which is determined by their volume fractions, distribution, mechanical properties, and especially morphology (curvatures). The enhancement in yield strength of the studied alloys $\Delta\sigma_{LT}$, benefiting from the load-bearing effect as indicated by the subscript LT, is described by the following equation^[33,44,50]:

$$\Delta\sigma_{LT} = \frac{1}{2} \times \sigma_m \times V_i \times s, \quad [7]$$

where σ_m is the yield strength of the base alloy, which is treated as 48.7 MPa according to Table V. In addition, s is the aspect ratio of the intermetallics. Considering the curvature distribution, s can be treated as 1. From the equation, it is obvious that the aspect ratio of intermetallics is the most critical factor because the volume fraction of intermetallics is fixed in most cases. In fact, the aspect ratio is related to K and H . Therefore, $\Delta\sigma_{LT}$ was calculated to be 5.36 MPa at 623 K (350 °C).

(d) Based on previous studies^[24,32] and this work, the interconnectivity of rigid intermetallics not only can improve the effect of load transfer, but also can enhance the load-carrying capacity through the homogenization of stress throughout the intermetallics with a 3-D consequent network structure. In addition, after the tensile test at 623 K (350 °C), the interconnectivity of the second phases in Al-6Cu-3.5Ni-0.8Fe-0.4Gd decreased by only ~ 2 pct (from ~ 98 to ~ 96 pct), remaining higher than that in Al-6Cu-3.5Ni. According to the above discussion, it can be inferred that the degree of interconnectivity of rigid intermetallics also plays a critical

Table VI. Previously Reported Mechanical Properties of Al Alloys at 623 K (350 °C) and Those Obtained in This Work

Composition (Wt Pct)	State	623 K (350 °C)		Ref.
		UTS (MPa)	EL (Pct)	
Al-6Cu-3.5Ni-0.8Fe-0.4Gd	as-cast	74.1 ± 1.2	15.5 ± 2.4	This work
Al-12.57Si-1.02Cu-1.23Mg-1.07Ni-0.04Mn	T6	67.07 ± 0.115	—	13
Al-12.57Si-1.02Cu-1.23Mg-1.07Ni-0.40Mn	T6	71.92 ± 0.556	—	13
Al-11.72Si-3.85Cu-1.94Ni-0.81Mg-0.16Fe-0.20Mn-0.49Gd	as-cast	70.5	9.76	21
Al-13.0Si-1.08Cu-1.05Mg-1.0Ni	T6	61.63	—	23
Al-12.8Si-3.23Cu-1.01Mg-1.0Ni	T6	61.71	—	23
Al-12.5Si-5.0Cu-0.84Mg-2.0Ni-0.5Fe-0.67Cr	T6	72.2	13.2	26
Al-14.43Si-3.93Cu-0.77Mg-2.67Ni-0.47Fe-0.17Mn-0.12Ti	T7	66.9 ± 1.5	10.1 ± 2.1	51
Al-14.43Si-3.93Cu-0.77Mg-2.67Ni-0.47Fe-0.17Mn-0.12Ti	T7	70.6 ± 1.0	4.0 ± 2.9	51
Al-17.77Si-3.82Cu-0.77Mg-2.74Ni-0.49Fe-0.19Mn-0.11Ti	T7	73.1 ± 2.1	3.0 ± 1.3	51
Al-12.15Si-3.32Cu-0.82Mg-2.51Ni-0.24Fe-0.59Mn-0.08Ti	T7	67.0 ± 0.9	9.9 ± 2.0	52
Al-12.81Si-4.17Cu-0.86Mg-2.26Ni-0.43Fe-0.35Mn-0.09Ti	T7	67.7 ± 0.7	3.7 ± 1.2	52
Al-11.97Si-3.79Cu-0.82Mg-3.39Ni-0.50Fe-0.18Mn-0.10Ti	T7	76.1 ± 2.3	9.1 ± 2.3	52
Al-11.85Si-3.73Cu-0.81Mg-1.97Ni-0.20Fe-0.16Mn-0.23Nd	as-cast	74.2	12.2	53
Al-11.94Si-3.95Cu-0.84Mg-1.98Ni-0.18Fe-0.17Mn-0.44Nd	as-cast	65.6	9.61	53
Al-12Si-3Cu-1.5Ni	as-cast	~ 61.4	~ 4.8	54
Al-13.5Si-3.8Cu-2Ni-1Mg-0.5Fe-0.2Mn-0.1Zn-1.0Zr	T6	69.50	3.89	55
Al-13.00Si-1.00Cu-1.00Mg-2.50Ni-0.35Zn	—	70 (588 K)	10 (588 K)	56
Al-13.00Si-1.30Cu-1.30Mg-1.50Ni-0.50Cr	—	73 (573 K)	—	56

role in the strengthening of the studied alloys at elevated temperatures. However, to date, there has been no quantitative formula for this mechanism. It is only known that the strengthening effect of this mechanism is positively related to the degree of interconnection, as confirmed by the strength comparison between Al-6Cu-3.5Ni-0.8Fe-0.4Gd alloy and Al-6Cu-3.5Ni alloy. In this paper, we only mark the yield strength enhancement of the studied alloys resulting from the degree of interconnectivity as $\Delta\sigma_I$.

To summarize, the total yield strength enhancement of the studied alloys can be summarized by the following equation:

$$\Delta\sigma_{\text{total}} = [\Delta\sigma_{\text{CTE}}^2 + \Delta\sigma_{\text{EM}}^2 + \Delta\sigma_{\text{OL}}^2]^{1/2} + \Delta\sigma_{\text{LT}} + \Delta\sigma_I. \quad [8]$$

Based on the discussion above, $\Delta\sigma_{\text{total}}$ can be calculated as 5.36 MPa + $\Delta\sigma_I$ at 623 K (350 °C). According to the YS of Al-6Cu-3.5Ni and Al-6Cu-3.5Ni-0.8Fe-0.4Gd at 623 K (350 °C) from Table IV, it can be inferred that $\Delta\sigma_I$ is approximately 7.14 MPa. In fact, the essence of both mechanisms (a) and (b) is dislocation movement. At elevated temperatures, the effects of both mechanisms (a) and (b) are severely weakened because of the rapid relaxation of the strain-hardened regions and dislocation climbing. On the other hand, mechanisms (c) and (d) play the most significant strengthening role when the temperature exceeds 573 K (300 °C). In other words, the formation of a 3-D continuous network structure of intermetallics through organization control has great potential for improving the high-temperature performance of Al alloys. Owing to the collaborative strengthening mechanism, the mechanical properties of the studied alloys at 623 K (350 °C) exceeded those

reported for many as-cast Al alloys, even after T6 treatment, as listed in Table VI.

V. CONCLUSIONS

The 3-D microstructure and mechanical properties of Al-6Cu-3.5Ni-0.8Fe cast alloys with different levels of Gd micro-addition were studied in this work. From the results presented above, the following conclusions can be drawn:

- (1) The XRD and EDS results revealed that the microstructures of the studied alloys consisted of α -Al, T -Al₉FeNi, ε -Al₃Ni, γ -Al₇Cu₄Ni, δ -Al₃CuNi, and Gd-rich phases, which were identified as Al₃CuGd. With increasing Gd content, the branches of δ -Al₃CuNi evolved to be smaller and denser, whereas disintegration and passivation were detected in T -Al₉FeNi.
- (2) Tensile tests at different temperatures indicated that the addition of Gd to the base alloy successfully improved the mechanical properties, especially the UTS and YS beyond 573 K (300 °C). Both at ambient and elevated temperatures, the alloy modified with 0.4 wt pct Gd exhibited the optimal strength. Specifically, the UTS at 623 K (350 °C) reached 74.1 MPa, which was more than 10.0 pct higher than that of the base alloy.
- (3) Fractographic analysis of the tested specimens indicated that brittle cleavage-type fracture dominated the entire tensile testing process in all of the studied alloys at room temperature. Simultaneously, numerous secondary cracks occurred in T -Al₉FeNi, revealing strong interfacial bonding between T -Al₉FeNi and the α -Al matrix.

However, with increasing Gd content, there was a transformation from mixed fracture to fully ductile trans-crystalline fracture at 623 K (350 °C). In addition, debonding and pull-out of T-Al₉FeNi and Al₃CuGd were detected simultaneously.

- (4) Compared with Al-6Cu-3.5Ni, Al-6Cu-3.5Ni-0.8-Fe-0.4Gd exhibited a higher strength at 623 K (350 °C), owing to the greater interconnectivity and curvature distribution close to the origin (0, 0). In addition, there was no significant decline in the interconnectivity of aluminides after tensile testing at 623 K (350 °C), which confirmed the excellent heat resistance of the 3-D continuous network structure formed in the studied alloy.
- (5) The strengthening mechanisms responsible for the high-temperature strength of the studied alloys were (i) dislocation strengthening from strain-hardened regions and the Orowan mechanism, (ii) load transfer from the matrix to aluminides, and (iii) the effect of the interconnectivity of the rigid 3-D network structure. It is worth mentioning that the 3-D network structure of rigid intermetallics explored in this work provide a new and promising ideas for solving the current heat resistance problems of cast Al alloys.

ACKNOWLEDGMENTS

The authors would like to acknowledge the financial support of the National Key R&D Plan (No. 2017YFB0703101) and the National Science Fund for Distinguished Young Scholars (No. 51425203) sincerely.

REFERENCES

1. R. Gholizadeh and S.G. Shabestari: *Metall. Mater. Trans. A*, 2011, vol. 42A, pp. 3447–58.
2. L. Lasa and J.M. Rodriguez-Ibabe: *Mater. Charact.*, 2002, vol. 48, pp. 371–78.
3. S.K. Shaha, F. Czerwinski, W. Kasprzak, J. Friedman, and D.L. Chen: *Mater. Sci. Eng. A*, 2015, vol. 636, pp. 361–72.
4. P. Srirangam, S. Chattopadhyay, A. Bhattacharya, S. Nag, and J. Kaduk: *Acta Mater.*, 2014, vol. 65, pp. 185–93.
5. M. Schöbel, G. Baumgartner, S. Gerth, J. Bernardi, and M. Hofmann: *Acta Mater.*, 2014, vol. 81, pp. 401–08.
6. F. Xia, X.S. Gao, M.X. Liang, Y.C. Guo, J.P. Li, Z. Yang, J.L. Wang, and L.L. Zhang: *J. Mater. Res. Technol.*, 2020, vol. 9, pp. 12926–35.
7. M. Abdulwahab, I.A. Madugu, and S.A. Yaro: *Mater. Des.*, 2011, vol. 32, pp. 1159–66.
8. J. Hernandez-Sandoval, G.H. Garza-Elizondo, A.M. Samuel, S. Valtierra, and F.H. Samuel: *Mater. Des.*, 2014, vol. 58, pp. 89–101.
9. A.M. Samuel, J. Gauthier, and F.H. Samuel: *Metall. Mater. Trans. A*, 1996, vol. 27A, pp. 1785–98.
10. J. Chen, E. Costan, and M.A. Van Huis: *Science*, 2006, vol. 312, pp. 416–19.
11. X.Y. Suo, H.C. Liao, Y.Y. Hu, U.S. Dixitb, and P. Petrov: *J. Mater. Eng. Perform.*, 2018, vol. 27, pp. 1–11.
12. H.C. Liao, Y.Y. Tang, X.Y. Suo, G.J. Li, Y.Y. Hu, U.S. Dixitb, and P. Petrov: *Mater. Sci. Eng. A*, 2017, vol. 699, pp. 201–09.
13. Z. Qian, X.F. Liu, D.G. Zhao, and G.H. Zhang: *Mater. Lett.*, 2008, vol. 62, pp. 2146–49.
14. S.K. Shaha, F. Czerwinski, W. Kasprzak, J. Friedman, and D.L. Chen: *Mater. Sci. Eng. A*, 2016, vol. 652, pp. 353–64.
15. M. Song, K.H. Chen, and L.P. Huang: *Trans. Nonferrous Met. Soc. China*, 2006, vol. 16, pp. 766–71.
16. D.H. Xiao, J.N. Wang, D.Y. Ding, and H.L. Yang: *J. Alloys Compd.*, 2003, vol. 352, pp. 84–88.
17. S.G. Shabestari: *Mater. Sci. Eng. A*, 2004, vol. 383, pp. 289–98.
18. A.K. Mukhopadhyay, G.J. Shiflet, and E.A. Starke: *Scr. Metall. Mater.*, 1990, vol. 24, pp. 307–12.
19. R.A. Karnesky, M.E. van Dalen, D.C. Dunand, and D.N. Seidman: *Scr. Mater.*, 2006, vol. 55, pp. 437–40.
20. X.G. Zhang, F.Q. Mei, H.Y. Zhang, S.H. Wang, C.F. Fang, and H. Hao: *Mater. Sci. Eng. A*, 2012, vol. 552, pp. 230–35.
21. Y.D. Sui, Q.D. Wang, T. Liu, B. Ye, H.Y. Jiang, and W.J. Ding: *J. Alloys Compd.*, 2015, vol. 644, pp. 228–35.
22. Y.D. Sui: Study on the microstructural and elevated temperature properties of cast Al-Si-Cu-Ni-Mg alloys. Doctor's thesis, Shanghai Jiao Tong University, China, 2016 (in Chinese).
23. Y.G. Li, Y. Yang, Y.Y. Wang, L.Y. Wang, and X.F. Liu: *Mater. Sci. Eng. A*, 2010, vol. 527, pp. 7132–37.
24. Z. Asghar, G. Requena, and F. Kubel: *Mater. Sci. Eng. A*, 2010, vol. 527, pp. 5691–98.
25. F.C. Meng, Y.Y. Wu, K.Q. Hu, Y. Li, and X.F. Liu: *Materials*, 2019, vol. 12, p. 2506.
26. Y.Y. Yang, S.Y. Zhong, Z. Chen, M.L. Wang, N.H. Ma, and H.W. Wang: *J. Alloys Compd.*, 2015, vol. 647, pp. 63–69.
27. J. Feng, B. Ye, L.J. Zuo, R.J. Qi, Q.D. Wang, H.Y. Jiang, R. Huang, and W.J. Ding: *Mater. Sci. Eng. A*, 2017, vol. 706, pp. 27–37.
28. G.J. Li, H.C. Liao, X.J. Suo, Y.Y. Tang, U.S. Dixit, and P. Petrov: *Mater. Sci. Eng. A*, 2018, vol. 709, pp. 90–96.
29. Y.G. Li, Y. Yang, Y.Y. Wu, Z.S. Wei, and X.F. Liu: *Mater. Sci. Eng. A*, 2011, vol. 528, pp. 4427–30.
30. G.J. Li, H.C. Liao, and A.Q. Xu: *Mater. Sci. Eng. A*, 2018, vol. 730, pp. 36–40.
31. L.J. Huang, L. Geng, H.X. Peng, and B.K. Aveyendran: *Mater. Sci. Eng. A*, 2012, vol. 534, pp. 688–92.
32. Z. Asghar, G. Requena, and E. Bollerb: *Acta Mater.*, 2011, vol. 59, pp. 6420–32.
33. H.B. Yang, S. Tian, T. Gao, J.F. Nie, Z.S. You, G.L. Liu, H.C. Wang, and X.F. Liu: *Mater. Sci. Eng. A*, 2019, vol. 763, pp. 138121.1–138121.11.
34. Y.D. Sui, Q.D. Wang, G.L. Wang, and T. Liu: *J. Alloys Compd.*, 2015, vol. 622, pp. 572–79.
35. R.V. Gumeniuk, B.M. Stel'makhovych, and Y.B. Kuz'ma: *J. Alloys Compd.*, 2001, vol. 329, pp. 182–88.
36. V. Raghavan: *J. Phase Equilib. Diffus.*, 2010, vol. 31, pp. 550–51.
37. N.A. Belov, D.G. Eskin, and N.N. Avxentieva: *Acta Mater.*, 2005, vol. 53, pp. 4709–22.
38. Muzaffer. Zeren: *Mater. Des.*, 2007, vol. 28, pp. 2511–17.
39. R.C. Atwood, J.R. Jones, P.D. Lee, and L.L. Hench: *Scr. Mater.*, 2004, vol. 51, pp. 1029–33.
40. A.M.A. Mohamed, F.H. Samuel, and S.A. Kahtani: *Materials*, 2013, vol. 577, pp. 64–72.
41. A.M.A. Mohamed, A.M. Samuel, F.H. Samuel, and H.W. Doty: *Mater. Des.*, 2009, vol. 30, pp. 3943–57.
42. N.C.W. Kuijpers, J. Tirel, D.N. Hanlon, and S. der Zwaaga: *Mater. Charact.*, 2002, vol. 48, pp. 379–92.
43. Y.D. Sui, D.P. Ji, L.N. Han, and Q.D. Wang: *J. Miner. Met. Mater. Soc.*, 2019, vol. 71, pp. 366–72.
44. M. Rashad, F.S. Pan, W. Guo, H. Lin, M. Asif, and M. Irfan: *Mater. Charact.*, 2015, vol. 106, pp. 382–89.
45. B.Q. Han and D.C. Dunand: *Mater. Sci. Eng. A*, 2000, vol. 277, pp. 297–304.
46. W.L.E. Wong and M. Gupta: *Compos. Sci. Technol.*, 2007, vol. 67, pp. 1541–52.
47. L. Jiang, H. Yang, J.K. Yee, X. Mo, T. Topping, E.J. Lavernia, and J.M. Schoenung: *Acta Mater.*, 2016, vol. 103, pp. 128–40.
48. S.P. Joshi and K.T. Ramesh: *Scr. Mater.*, 2007, vol. 57, pp. 877–80.

49. M.E. van Dalen, D.C. Dunand, and D.N. Seidman: *Acta Mater.*, 2005, vol. 53, pp. 4225–35.
50. Z.H. Zhang, T. Topping, Y. Li, R. Vogt, Y.Z. Zhou, C. Haines, J. Paras, D. Kapoor, J.M. Schoenung, and E.J. Lavernia: *Scr. Mater.*, 2011, vol. 65, pp. 652–55.
51. J.-G. Jung, J.-M. Lee, Y.-H. Cho, and W.-H. Yoon: *J. Alloys Compd.*, 2017, vol. 693, pp. 201–10.
52. J.-G. Jung, S.-H. Lee, Y.-H. Cho, W.-H. Yoon, T.-Y. Ahn, Y.-S. Ahn, and J.-M. Lee: *J. Alloys Compd.*, 2017, vol. 712, pp. 277–87.
53. L. Han, Y. Sui, Q. Wang, K. Wang, and Y. Jiang: *J. Alloys Compd.*, 2017, vol. 695, pp. 1566–72.
54. L. Zuo, B. Ye, J. Feng, X. Xiaojing, X. Kong, and H. Jiang: *J. Alloys Compd.*, 2019, vol. 791, pp. 1015–24.
55. T. Gao, X. Zhu, Q. Sun, and X. Liu: *J. Alloys Compd.*, 2013, vol. 567, pp. 82–88.
56. E.R. Wang, X.D. Hui, and G.L. Chen: *Mater. Des.*, 2011, vol. 32, pp. 4333–40.

Publisher's Note Springer Nature remains neutral with regard to jurisdictional claims in published maps and institutional affiliations.